Journal of
Materials Chemistry C

ROYAL SOCIETY
OF CHEMISTRY

PAPER

View Article Online
View Journal | View Issue

Check for updates

Cite this: *J. Mater. Chem. C*, 2025, **13**, 17353

Influence of pore-confined water on the thermal expansion of a zinc-based metal–organic framework†

Nina Strasser,[a] Benedikt Schrode,[b] Ana Torvisco,[c] Sanjay John,[a] Birgit Kunert,[a] Brigitte Bitschnau,[d] Florian Patrick Lindner,[a] Christian Slugovc,[e] Egbert Zojer*[a] and Roland Resel*[a]

Received 30th April 2025,
Accepted 15th July 2025

DOI: 10.1039/d5tc01746g

rsc.li/materials-c

Understanding the reversible intercalation of guest molecules into metal–organic frameworks is crucial for advancing their design for practical applications. In this work, we explore the impact of H_2O as a guest molecule on the thermal expansion of the zinc-based metal–organic framework GUT-2. Dehydration is achieved by thermal treatment of hydrated GUT-2. Rietveld refinement performed on temperature-dependent X-ray powder diffraction data confirms the reversible structural transformation. Additionally, it allows the determination of anisotropic thermal expansion coefficients for both forms. The hydrated form exhibits an extremely small thermal expansion along the polymer chain direction moderate expansion in the direction of predominantly hydrogen bonds, and the highest expansion in the direction with only van der Waals bonding. Upon activation, the removal of H_2O molecules triggers a doubling of the thermal expansion coefficient in the direction, where the hydrogen bonds have been removed. Regarding the dynamics of the process, thermal activation in air occurs within 6 hours at a temperature of 50 °C and takes only 30 minutes when heating to 90 °C. In contrast, full rehydration under standard lab conditions (30% relative humidity) requires two days. During the activation/dehydration processes no change of the widths of the X-ray diffraction peaks is observed, which shows that the underlying crystal structure remains intact during the transition processes. Fitting the transformations by the Avrami equation reveals a quasi one-dimensional evolution of the dehydrated areas for the activation process and a more intricate, predominantly two-dimensional mechanism for the rehydration.

1. Introduction

According to the IUPAC recommendation, a metal–organic framework (MOF) is a "coordination network with organic ligands containing potential voids".[1] These voids (often also called pores) can trap small molecules, a process that can fundamentally change the functionality of the MOF. In catalysis, for instance, MOFs can encapsulate molecular catalysts, shielding them from reactive species and preventing deactivation during the chemical reaction.[2–4] Moreover, MOFs can encapsulate enzymes, preventing their denaturation,[5] or can hold drug molecules, enabling their controlled release for maximizing the therapeutic responses.[6] MOFs are also promising candidates for electronic sensors, in which they serve as adsorption systems for gas molecule detection.[7,8] Interaction of MOFs with small molecules can, however, pose significant risks to their structural integrity. For example, several systems belonging to the isoreticular MOF family[9] (which is a series of MOFs that have a similar network topology) including MOF-5[10,11] disintegrate after minimal exposure to H_2O. The primary reason is that H_2O molecules can easily hydrolyse the relatively weak metal–organic coordination bonds. This then leads to the structural collapse of the whole framework. However, there are also MOFs which show exceptional H_2O resistance, a feature that aligns with the recent development of innovative MOFs that allow harvesting H_2O from atmospheric moisture, even amidst desert conditions.[12,13]

Generally speaking, H_2O adsorption in MOFs involves interactions that vary in strength depending on the binding sites and the specific framework structure.[14] In some cases, H_2O is weakly bound through hydrogen bonding, allowing for

---

[a] *Institute of Solid State Physics, NAWI Graz, Graz University of Technology, Petersgasse 16, 8010 Graz, Austria. E-mail: egbert.zojer@tugraz.at, roland.resel@tugraz.at*

[b] *Anton Paar GmbH, Anton-Paar-Straße 20, 8054 Graz, Austria*

[c] *Institute of Inorganic Chemistry, NAWI Graz, Graz University of Technology, Stremayrgasse 9, 8010 Graz, Austria*

[d] *Institute of Physical and Theoretical Chemistry, NAWI Graz, Graz University of Technology, Stremayrgasse 9, 8010 Graz, Austria*

[e] *Institute of Chemistry and Technology of Materials, NAWI Graz, Graz University of Technology, Stremayrgasse 9, 8010 Graz, Austria*

† Electronic supplementary information (ESI) available. CCDC 2406179 and 2406180. For ESI and crystallographic data in CIF or other electronic format see DOI: **https://doi.org/10.1039/d5tc01746g**

reversible adsorption and desorption, such as in the aforementioned H_2O-harvesting applications.[15] Conversely, certain MOFs exhibit binding sites, where H_2O molecules are so strongly coordinated (*e.g.*, *via* metal centres or specific functional groups) that H_2O desorption becomes rather challenging.[16] These differences in binding strengths influence the structural responses of the framework to both H_2O inclusion or desorption, leading to diverse effects that can range from simple expansions or contractions of the framework to more complex phenomena, such as ligand rearrangements or phase transitions. These responses have direct crystallographic consequences, such as modifications of cell parameters, changes in symmetry, or the reorientation of linkers.[17]

Alternative processes modifying the details of MOF structures in response to temperature changes are thermal expansion processes. In MOFs they occur in (a combination of) three flavours: (i) the most common response to changes in temperature is a positive thermal expansion (PTE), where the cell dimensions expand upon heating.[18–20] (ii) A less frequent phenomenon is negative thermal expansion (NTE), where cell dimensions decrease with increasing temperature (at least in one of the crystallographic directions).[21–23] (iii) Finally, a material may exhibit zero thermal expansion (ZTE), where the cell dimensions remain essentially unchanged with temperature.[24,25] The condition for ZTE is that one thermal expansion coefficient is smaller than $1 \times 10^{-6}\ \mathrm{K}^{-1}$.[26] ZTE is, for example, highly desirable in the design of materials for high-precision devices, where maintaining a constant shape and size across multiple temperature ranges is crucial for maintaining the accuracy of the device.[27]

Interestingly, it has been shown that the aforementioned adsorption of guest molecules can be used to control thermal expansion processes.[28–30] For instance, a lanthanide-based MOF incorporating dimethylformamide (DMF) molecules within its pores exhibited tuneable NTE attributed to a reduction in pore sizes upon guest molecule removal.[31] Another study on $Zn_2(BDC)_2(DABCO)$ compared the thermal expansion of the MOF containing DMF molecules with that of the system containing benzene as guest molecules.[32] This revealed distinct host–guest interactions likely responsible for varied thermal responses, as further supported by a study on a Zn-based MOF highlighting the role of pore-filling molecules in tuning thermal expansion behaviour.[33] In yet another case, the MOF PCN-222 along one axis displayed a thermal expansion coefficient that changed its sign depending on the H_2O content within its pores.[34] While these previous studies have explored the role of guest molecules in influencing the thermal expansion of MOFs, a comprehensive understanding of how specific bonding interactions and structural rearrangements contribute to anisotropic thermal expansion remains limited – a gap this study aims to address.

Studying the intimate interplay between thermal expansion and guest adsorption is in the focus of the current manuscript. The experiments are performed on GUT-2,[35] a Zn-based MOF recently developed at Graz University of Technology. It has been chosen for this study for a variety of reasons: (i) GUT-2 is stable in H_2O and humid environments, (ii) it can be activated and rehydrated without framework degradation in a reversible process, (iii) it can be rather straightforwardly grown into comparably large single crystals, which allows the exact determination of its atomistic structure, and (iv) it has a well-defined binding site for H_2O molecules, at which they can form linkages between strands of the GUT-2 coordination polymer *via* establishing hydrogen bonds.

2. Experimental details

2.1. Synthesis

GUT-2 was synthesized in an aqueous solution following the protocol reported in ref. 35. After synthesis, the obtained white powder was dried by blowing a stream of N_2 gas over it.

2.2. Single crystal X-ray diffraction

The measurements of GUT-2 were performed on a Rigaku XtaLAB Synergy, Dualflex, HyPix-Arc 100 diffractometer equipped with an Oxford Cryosystems cryostream. A single crystal was selected from the as-synthesized (hydrated) powder and carefully mounted on a glass rod on a metal pin and secured with glue (Loctite Super Attack) to ensure that the single crystal would not detach during the measurement. The glue was pre-tested to confirm that it contained no crystalline components, which would interfere with the diffraction experiment. Data were collected at −173 °C (100 K) for hydrated GUT-2. The measurements of activated GUT-2 (373 K) were also performed directly on the instrument at an elevated temperature of 100 °C, utilizing the cryostream with activation achieved *in situ* starting from the hydrated single crystal.

For the measurement, Cu Kα radiation (λ = 1.54056 Å) was used. The diffraction pattern was indexed and the total number of runs and images was based on the data collection strategy calculated by the program CrysAlisPro[36] (with all details available in the provided CIFs). The unit cell was refined and data reduction, scaling, and absorption corrections were performed with this program. Using OLEX2,[37] the structure was solved with the SHELXT structure solution program[38] and refined with the SHELXL refinement package[39] using full matrix least squares minimization on F^2. All non-hydrogen atoms were refined anisotropically. Hydrogen atom positions were calculated geometrically and refined using the riding model. Activated GUT-2 (373 K) was refined as a 2-component twin (BASF 0.39). It showed comparably weak and diffuse Bragg scattering, which is related to the fact that the structure was collected at 373 K, which contributes to enlarged displacement parameters, indicative of an increased thermal motion of the atoms in accordance with data collection at higher temperature (see ESI† for more details).

CIF files were edited, validated and formatted either with the programs enCIFer,[40] publCIF[41] or OLEX2.[37] CCDC 2406179 and 2406180 contain the supplementary crystallographic data for hydrated GUT-2 (compound (**1**)) and for activated GUT-2 (compound (**2**)), respectively. Table S1 (ESI†) contains crystallographic data and details of measurements and refinements for compounds (**1**) and (**2**).

2.3. Powder X-ray diffraction – thermal expansion

Powder X-ray diffraction (PXRD) experiments for determining thermal expansion coefficients were performed with the XRDynamic 500 diffractometer from Anton Paar equipped with a Primux 3000 sealed-tube X-ray source with Cu anode (λ = 1.5418 Å) and a Pixos 2000 detection unit featuring a solid-state pixel detector with Si sensors operated in 1D mode. Data were collected in Bragg–Brentano beam geometry with a primary flat multilayer X-ray mirror from 10° to 50° 2θ with a step size of 0.01°. Soller slits with an opening of 0.05 rad were used on the primary and secondary side.

The cooling of the finely-grinded, as-synthesized GUT-2 sample was achieved using the low-temperature attachment TTK600 from Anton Paar Ltd. Graz under vacuum conditions (1×10^{-3} mbar) using liquid N_2 as a cooling agent. Starting from 25 °C the sample was cooled/heated in steps of 50 °C with a cooling/heating rate of 2 °C min^{-1}. Waiting times and automatic sample alignments were applied at each temperature step to ensure homogeneous sample temperature and sample alignment. The actual temperature curves contain plateaus of constant temperatures at each set of the set points for 20 minutes in order to allow the temperature to equilibrate (see Fig. S13 in the ESI†). During the refilling of liquid N_2 at 25 °C, moisture infiltrated into the supply line. This moisture subsequently froze, leading to a reduction in the cooling efficiency during the second cooling run, limiting the lowest achievable temperature to −180 °C.

In order to obtain the anisotropic thermal expansion coefficients from the temperature-dependent PXRD patterns, Rietveld refinements[42] were performed using the program X'Pert Highscore Plus[43] (Version: 3.0). The structural models used for the refinements were the crystal structure solutions obtained by single-crystal XRD experiments. The profile parameters that were included in the refinements are the zero shift, an overall scale factor, the three cell lengths as well as the line broadening parameters U, V and W of the Caglioti function.[44–46] Moreover, the background contributions were modelled using a polynomial function, while the peak-shape function is represented by a pseudo-Voigt function. The diffracted intensities were corrected for preferred orientation effects, which indicated that the (010) plane in the hydrated form is preferentially aligned parallel to the sample holder base.[47] For the activated from the orientation stays the same, but when applying the Niggli naming convention[48] for the crystallographic directions, this means that now the (001) plane would be aligned parallel (see discussion below). The full width at half maximum (FWHM) is then calculated as the peak width where the peak intensity falls to fifty percent of its maximum value.

2.4. Powder X-ray diffraction – activation and hydration kinetics

Temperature-dependent PXRD measurements for studying the kinetics of activation and rehydration were performed on a PANalytical Empyrean system in combination with a sealed copper tube and using a DHS900 heating attachment[49] from Anton Paar. For all powder diffraction experiments, GUT-2 powder finely grinded in a porcelain mortar was put on a silicon wafer. The primary X-ray beam was monochromatized and parallelized by an X-ray mirror. The diffracted beam was detected by a 1-dimensional detector mode using a PIXcel3D detector with 255 active channels. In this mode, the detector simultaneously records diffraction intensities along a single axis (2θ). An anti-scatter slit of 7.5 mm and a 0.02 rad Soller slit were used. Careful alignments of the sample height were performed at each temperature to obtain reliable diffraction patterns. The relative humidity was measured using a hygrometer.

3. Results and discussion

3.1. X-ray diffraction characterization of the thermally-induced activation

Macroscopically, hydrated GUT-2 is a crystalline, white powder. At an atomistic level, it consists of individual strands of a coordination polymer, connected by H_2O molecules as illustrated in Fig. 1(a)–(c). These H_2O molecules form hydrogen bonds of the type $O\cdots H_w–O_w–H_w\cdots O$ (with atoms being part of the H_2O molecule denoted by the subscript 'w') between the oxygen atom belonging to the carboxylate groups of the linkers. The individual strands of GUT-2 consist of Zn^{2+} metal centres that are connected *via* 3-(2-methyl-1*H*-imidazole-1-yl)propanoate linkers. Each Zn^{2+} ion is surrounded by two oxygen atoms from the carboxylate groups and two nitrogen atoms from the 2-methyl-imidazolate ring, forming a tetrahedral geometry with a coordination number of four. Overall, the crystal structure solution of hydrated GUT-2 that we obtained by single-crystal diffraction is fully consistent with the one proposed in ref. 35. This is shown by a direct comparison of the two sets of crystallographic data (see Table 1), which testifies to the reproducibility of the GUT-2 synthesis.

The activation of GUT-2 can be performed, for example, by heat treatment. The H_2O molecules in hydrated GUT-2 efficiently leave the framework pores, for example, at a temperature of 50 °C (with details on the kinetics of the process discussed in Section 2.3). This results in completely dehydrated but still intact, colorless, block-shaped single crystals. The activated form of GUT-2 (like the hydrated one) crystallizes in an orthorhombic crystal system, the space group changes from *Pcca* to *Pccn* and the primitive unit cell significantly contracts in two directions for the activated form (see Table 1).

Calculating the volumes of the unit cells listed in Table 1 yields a shrinkage by a factor of more than 2. At first glance, this appears like a drastic change; a closer inspection of the single crystal diffraction data, however, reveals that it is primarily a consequence of a reduction of the number of chemical formula units per unit cell by a factor of 2. This is the consequence of a minor rearrangement of the pores due to removal of the direct connections between neighboring strands as a consequence of the desorption of the H_2O molecules. In turn the translational periodicity in the plane perpendicular to the polymer chains (*i.e.*, in the *ac*-plane) changes: the unit cell

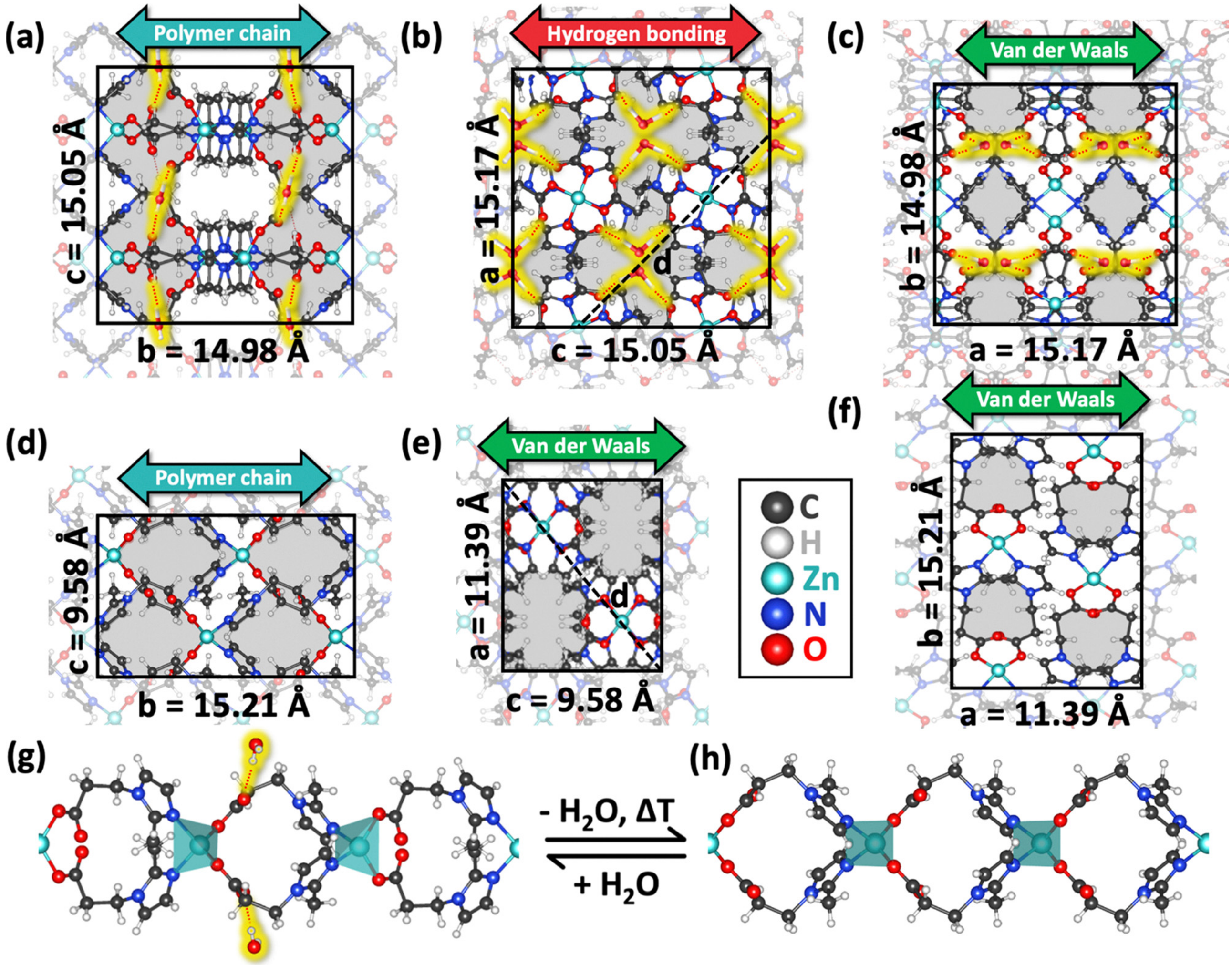

Fig. 1 Framework structure within the orthorhombic crystal structures of hydrated (a)–(c) and activated GUT-2 (d)–(f) along all three unit cell axes. Hydrogen bonding in the hydrated form is indicated using red dotted lines (highlighted in yellow) connecting water molecules (also highlighted in yellow) to oxygen atoms in the carboxylates. Pores are shaded in grey. Double-sided arrows indicate the type of chemical bonding dominating in specific directions. Black, dashed lines indicate the diagonal *d* that will become relevant in the later discussion. Moreover, a single polymer strand of hydrated GUT-2 (g) and of its activated form (h) is projected along the axis connecting the centres of two adjacent pores. Transparent cyan polyhedra show the tetrahedral bonding situations around the Zn^{2+} ions. The illustrations visualizing the crystal structures are generated using OLEX2 (version 1.5).[34] Please note that for naming the crystallographic directions in the activated form we do not use the Niggli naming convention,[53] as discussed in detail in the caption of Table 1.

of the hydrated form in Fig. 1(b) contains four (partly blocked) channels shown as grey-shaded areas, which run in *b*-direction (*i.e.*, in the direction parallel to the polymer chains). Conversely, in the activated form shown in Fig. 1(e) only two (now completely open) channels are contained. Moreover, the unit cell in the *ac*-plane is rotated such that the *a* and *c* directions of the activated form run roughly parallel to the diagonals of the unit cell in the hydrated form and *vice versa*. Still, even when considering the factor of two arising from the modified translational periodicity, the volume of the unit cell of the activated form is reduced by around 3%. This occurs despite the considerably higher temperature at which the unit cell of the activated form has been determined (100 °C *vs.* −173 °C for the hydrated form). The volume reduction occurs also despite the loss of H-bonding between polymer strands in *c*-direction and is, thus, primarily attributed to the H_2O molecules not only strengthening the bonding between polymer strands but also serving as (weak) spacer units. Additionally, the removal of H_2O molecules results in slight changes of the linker alignments (see panel (g) and (h) of Fig. 1), resulting in a rotation of the 2-methyl-imidazolate linkers coordinated to the Zn^{2+} ions. This also changes the methyl group orientation on the imidazole rings. The overall extent of these rearrangements is, however, rather minor, which indicates that the fundamental framework structure remains largely intact upon thermal activation. From a practical point of view, the most relevant difference between both forms of GUT-2 is that in the hydrated form the hydrogen-bonded H_2O molecules block the pores running in the directions of the polymer strands (Fig. 1(b)), which is no longer the case in the activated form (see Fig. 1(e) and also Fig. S1 in the ESI†).

Table 1 Structural parameters for the hydrated and activated form of GUT-2 according to single crystal X-ray diffraction measurements. Please note that in naming the different crystallographic directions for the activated form, we do not follow the Niggli naming convention[48] to allow a more direct comparison to the structural parameters (including thermal expansion coefficients) of the hydrated form. The cell parameters (*a*, *b* and *c*) following Niggli convention are, thus, provided in brackets. The parameter *Z* denotes the number of (chemical) formula units within the unit cell. For the hydrated form, the single crystal structure solution exhibits a residual value (R_1) of 2% (for definition of R_1 see Section S2 in the ESI) when considering reflections for which the intensity satisfies the condition $I \geq 2\sigma$. This means that only reflections where the measured intensity exceeds twice its estimated standard deviation are included in the calculation. In contrast, the activated form of GUT-2 at 100 °C yields a higher R_1 value of 8%, which can be attributed to the elevated temperature at which the measurement has been performed. For a more in-depth discussion of this topic, the reader is referred to Section S2 in the ESI (especially Fig. S2), where also a more extensive version of this table is provided

	Hydrated GUT-2 (−173 °C)[35]	(1) Hydrated GUT-2 (−173 °C)	(2) Activated GUT-2 (100 °C)
Formula	$C_{14}H_{18}N_4O_4Zn{\cdot}H_2O$	$C_{14}H_{18}N_4O_4Zn{\cdot}H_2O$	$C_{14}H_{18}N_4O_4Zn$
Weight [g mol^{-1}]	389.73	389.71	371.69
Temperature [K]	100	100	373
a [Å]	15.1861(13)	15.1721(3)	11.3850(7) [*b*]
b [Å]	15.0082(13)	14.9839(3)	15.2053(7) [*c*]
c [Å]	15.0568(13)	15.0445(3)	9.5687(6) [*a*]
$\alpha = \beta = \gamma$ [°]	90	90	90
Volume [Å^3]	3431.7(5)	3420.17(12)	1656.46(16)
Z	8	8	4
Crystal system	Orthorhombic	Orthorhombic	Orthorhombic
Space group	*Pcca*	*Pcca*	*Pccn*
Crystal size [mm^3]	0.05 × 0.05 × 0.04	0.17 × 0.12 × 0.09	0.17 × 0.12 × 0.09
R_1, wR_2 ($I \geq 2\sigma$)	0.0212, 0.0533	0.0344, 0.0785	0.0839, 0.2335

Despite this opening of additional channels in the activated form of GUT-2, the void space of the material calculated by the contact surface method[49] on the basis of the single crystal structure (as implemented in Mercury[50] (version: 2024.2.0)) hardly changes upon activation. It remains at a comparatively low value of roughly 2%. This is in sharp contrast to the pronounced pore-opening transition observed, for example, in MIL-53 upon exposure to a variety of gases.[51,52] These different behaviors of GUT-2 and MIL-53 are not unexpected considering that here we are dealing with a system consisting of essentially 1D coordination polymer strands held together mostly by van der Waals forces and hydrogen bonds, while MIL-53 is a highly porous 3D-connected MOF. From the contact surface analysis[53] we can also conclude that the voids in GUT-2 can accommodate molecules with a maximum probe radius of 1.2 Å. When choosing larger probe sizes, we do not observe any detectable voids. This is insofar relevant, as it indicates that both forms of GUT-2 lack sufficient space to host additional H_2O molecules, which are typically associated with a probe radius of 1.4 Å.[54]

As a further validation of the structures determined by single crystal X-ray diffraction, we also performed geometry optimizations using state-of-the-art dispersion-corrected density functional theory. As detailed in the ESI,† these simulations yield only very minor changes of the lattice constants. These minor deviations are at least in part caused by the fact that the simulations are performed at essentially 0 K. Also, the positions of the atoms within the unit cell remain virtually the same indicating that the proposed structures represent stationary points of the potential energy surface of GUT-2.

Additionally, we verified the mechanical stability of both GUT-2 structures by testing the Born stability criterion,[55] which is based on the elastic tensor elements of the structures. In passing we note that in a recent work, some of us managed to extract elements of the elastic tensor of the hydrated GUT-2 structure, *via* a combination of Brillouin light scattering spectroscopy and theoretical methods, yielding excellent agreement between experiment and theory.[56] Using the results from that study and calculating the elastic constants also for activated GUT-2, one can show that the Born stability criterion[55] is fulfilled for both structural solutions from Table 1. This testifies to their mechanical stability (see Section S10, ESI†).

The following experiments were carried out to determine the thermal expansion of GUT-2 in its hydrated and activated forms and to analyze its activation and hydration kinetics. They were performed on isotropic powder samples. This is motivated by the fact that powder diffraction experiments provide phase-averaged structural information, minimizing the impact of local inhomogeneities or domain effects.[57]

Before discussing thermal expansion, a crucial aspect needs to be addressed that will be central to our analysis of the anisotropic thermal expansion coefficients: the different types of chemical bonding types present in GUT-2. The hydrated form of GUT-2 features three distinct types of interactions, as highlighted in Fig. 1 using double-sided arrows: (i) covalently linked polymeric chains extending along the *b*-direction, (ii) a network of hydrogen bonds along the *c*-direction that link polymer chains into 2D sheets, and (iii) van der Waals interactions along the *a*-direction. The latter represent the weakest type of bonding, but still, they significantly contribute to the overall cohesion of the structure. Upon activation, in which H_2O molecules are removed, the polymer chain backbone remains oriented along the *b*-direction, maintaining the primary structural integrity of the MOF. However, due to the absence of H_2O molecules, hydrogen bonds cease to exist. As a result, a structural rearrangement occurs, such that after activation polymer chains are held together primarily by van der Waals interactions in all directions perpendicular to the *b*-direction. Notably, these van der Waals interactions play a crucial role in determining the mechanical properties of materials, as previously discussed in the context of two-dimensional MOFs.[58] Importantly,

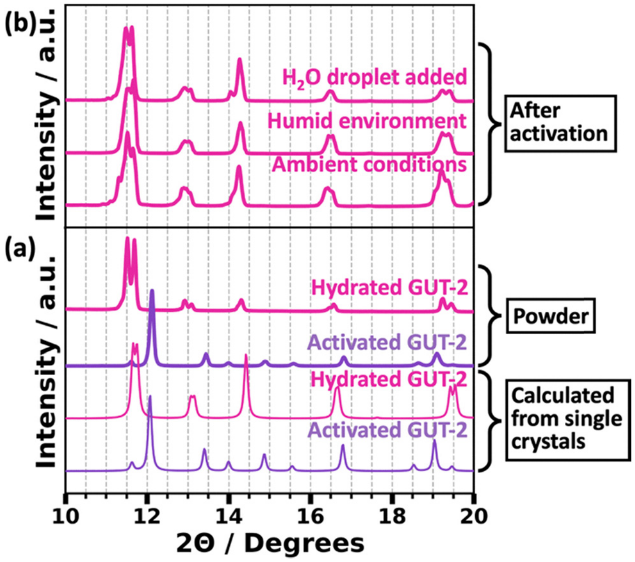

Fig. 2 Powder X-ray diffraction (PXRD) patterns of GUT-2 in various stages of activation. PXRD patterns shown by thick lines are experimentally measured curves, while thinner curves correspond to simulated data. In panel (a), diffractograms of activated GUT-2 (purple curve) and hydrated GUT-2 (pink curve) determined calculated based on the single crystal diffraction data are compared to powder patterns of hydrated GUT-2 measured right after the synthesis and after activation by thermal treatment. Additionally, panel (b) contains the diffractograms for the activated powder left at ambient conditions (relative humidity of 30% and a temperature of 25 °C) for two weeks, for the powder stored in humid environment (relative humidity of 100%) for two days, and for the powder after direct treatment with a drop of water.

these van der Waals interactions do not remain identical to those in the hydrated form, as the framework adjusts to compensate for the loss of hydrogen bonding, thereby altering the overall bonding environment (see above discussion).

To interpret the powder data, we calculated the expected powder diffractograms of hydrated and activated GUT-2 based on the single crystal results using Mercury[50] (version: 2024.2.0). They are shown in Fig. 2(a) as thin pink and purple lines, respectively. Their peak positions agree very well with the diffractogram of the studied powder (thick pink curve) achieved by grinding the as-synthesized material using a porcelain mortar (see Method section) and a powder achieved by activating the MOF in vacuum at 100 °C for 12 hours (thick purple curve). Minor differences in peak positions are attributed to the different temperatures at which the structures were measured: the single crystal data for the hydrated form of GUT 2 were determined at −173 °C and those for the activated form at 100 °C (see above), while the powder patterns were measured at room temperature. Interestingly, after activation the dehydrated GUT-2 powder can be rehydrated in a variety of ways. This is illustrated in Fig. 2(b) for the case of leaving the sample for two weeks at typical lab conditions (∼30% humidity), for the case of keeping the sample in a sealed vessel containing H_2O at the base (100% humidity) and for putting a drop of H_2O on top of the sample, which causes an instantaneous conversion back to the hydrated form. Overall, the diffractograms for all these cases agree very well with that of the as synthesized form. Minor deviations, for example, for the diffractogram of the sample rehydrated over two weeks at ambient conditions suggest a certain level of defects introduced by extended (de)hydration cycles.

3.2. Varying sample temperature and hydration state

The ability of GUT-2 to undergo a reversible reaction to switch between its hydrated and activated crystal structure makes it an ideal system to study the impact of the presence of guest molecules on the thermal expansion of MOFs. To determine the anisotropic thermal expansion coefficients of GUT-2, temperature-dependent PXRD measurements were performed. The temperature curves for the sample treatment are shown in Fig. 3(a). Starting from the hydrated form at 25 °C, the experiment followed a sequence of two sets of cooling and heating cycles (C1 and H1 as well as C2 and H2). Between the two sets of cycles the originally (partially) hydrated GUT-2 was thermally activated by keeping the sample at 100 °C for 12 hours. This yielded diffractograms for one cooling and one heating cycle for each form (hydrated and activated). The lowest temperature reached in C1 was −190 °C. The highest temperature reached during H2 was 250 °C, a temperature that is just below the decomposition temperature of GUT-2, which has been reported to be 270 °C.[35]

The most prominent diffraction features of the hydrated form are clearly resolved (and indexed) during the cycles C1 and H1. Comparing the temperature-dependent diffraction patterns in Fig. 3(b) and (c) with Fig. 3(d) and (e) reveals that all peaks observed after GUT-2 activation are also present (with lower intensities) before the annealing at 100 °C. Notably, the most prominent peak associated with the activated form (the (110) peak at 12.1 degrees) as well as the peak at 13.4 degrees (the (111) peak of the activated form) intensify with heating during process step H1. In contrast, during the initial cooling C1 only a very minor change in the relative peak intensities is observed. This suggests that partial activation of the powder has occurred already during the preliminary test-runs prior to the actual C1 measurements and this activation continues during the heating in processing step H1 (for further details see Fig. S10 in the ESI†).

After the thermal annealing, none of the X-ray diffraction features associated with the hydrated form of GUT-2, as indicated by the dashed lines in Fig. 3(b) and (d), are visible any more. Rather, only diffraction peaks expected for the fully activated form are observed, which suggests a full activation of the sample. To verify that the aforementioned pre-activation of the MOF sample has indeed occurred and to comprehensively analyze all structural data obtainable from the diffractograms, Rietveld refinements are performed. A comparison of the Rietveld refinements of the C2 and H1 measurements at a temperature of −150 °C – the lowest common temperature – is shown in Fig. 3. Rietveld refinements at all other temperature set points are given in Fig. S4–S9 (ESI†) for all four temperature curves, while Tables S11–S14 (ESI†) list the statistical parameters assessing the quality of the fits. There, also a

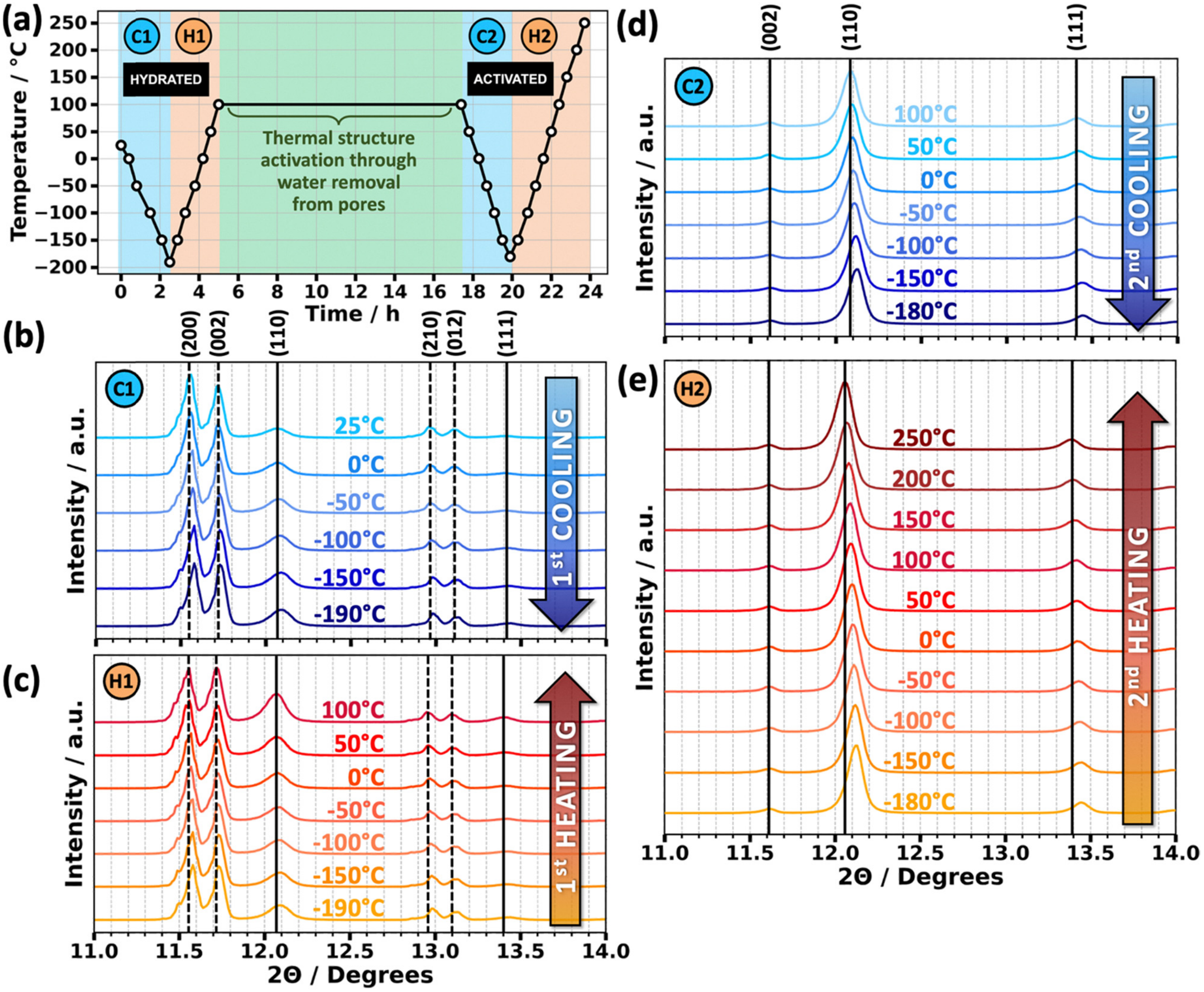

Fig. 3 (a) Temperature sequence for powder X-ray diffraction study of hydrated and activated GUT-2 at fixed set points (black circles). The first cooling curve (C1) for the hydrated form starts at room temperature (25 °C) and cools down to a temperature of −190 °C. This is followed by the first heating curve (H1) where, the sample is heated to up to 100 °C. Subsequently, the sample is held at this this temperature for 12 h to fully activate GUT-2 by dehydrating the pores. Subsequently, the activated sample undergoes a second cooling cycle (C2) down to −180 °C, followed by a final heating cycle (H2) up to 250 °C. (b)–(e) show temperature-dependent diffraction pattern in the 2θ range between 11 degrees and 14 degrees obtained from both heating and cooling curves. Peaks associated with hydrated GUT-2 are highlighted by dashed vertical lines, whereas solid vertical lines indicate the peaks of the activated form. These lines represent the peak position at the highest temperature. All these experiments were performed in vacuum.

more in-depth discussion of the quality of the fits and the mathematical definition of the statistical parameters can be found.

In short, in the context of Rietveld refinement, the parameter R_p, or profile residual, serves as a metric for assessing the agreement between experimental and simulated diffraction data.[59] It is defined as the sum of the absolute differences between observed and calculated intensities, divided by the total observed intensity. While a lower R_p value suggests a better fit, it should be interpreted with caution, as it does not consider factors such as background noise or preferred orientations. The most straightforward refinement can be done for the diffractogram shown in Fig. 4(c), where the crystal structure of activated GUT-2 serves as an ideally suited refinement model. The R_p value for this refinement amounted to 17.4%. Compared to typical R_p values for well-ordered crystalline materials, this might appear rather large, but in the present case It is most likely just caused by the deviation from a perfectly isotropic arrangement of the crystallites. The Rietveld refinement of the H1/C1 diffraction pattern using only the hydrated model (Fig. 4(a)) provides an incomplete description of the data, leaving key experimental peaks unexplained. Incorporating the activated form of GUT-2 as a secondary phase significantly enhances the fit (Fig. 4(b) and Fig. S5, S7, ESI†). Phase quantification shows that during each cooling cycle (prior to full activation), approximately 8% of the sample are activated in the temperature range from 25 °C to −50 °C over a timespan of 2 hours, with no additional activation occurring at lower temperatures (see also Fig. S10, ESI† and associated discussion). During the first heating curve an additional

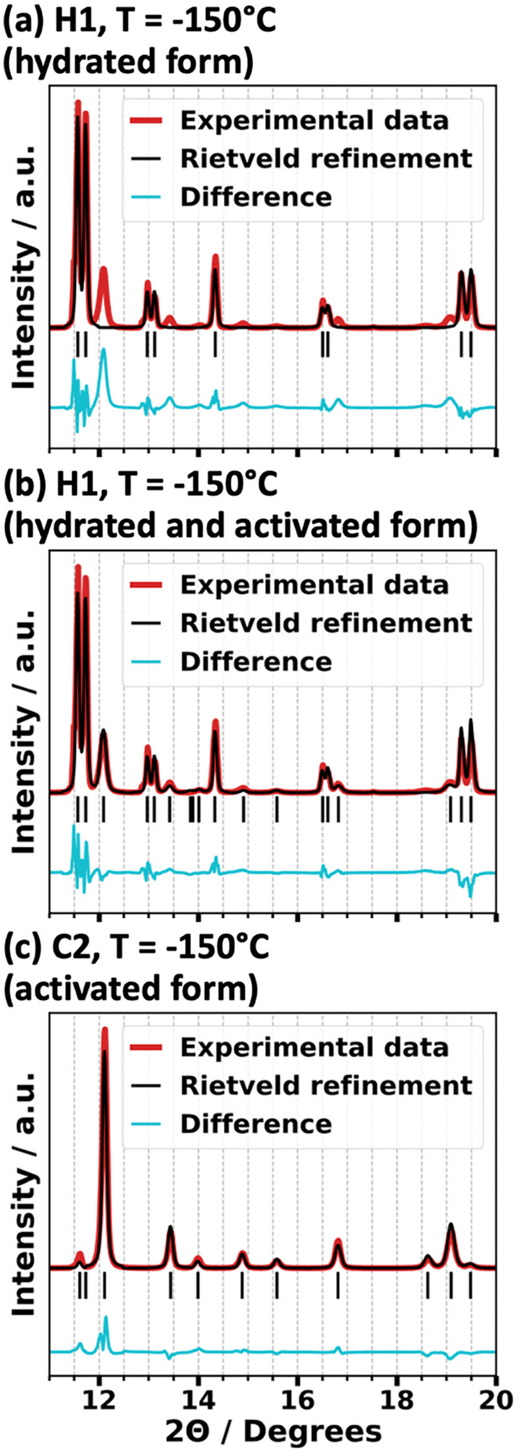

Fig. 4 Overlay of the powder X-ray diffraction patterns (red curves) measured at −150 °C and Rietveld refinements (black curves). Panel (a) corresponds to the first heating curve (H1) using only the hydrated form of GUT-2 as a model, while panel (b) includes both the activated and hydrated forms of GUT-2. The Rietveld refinement of the second cooling curve (C2) shown in panel (c) was performed using only the structure of activated GUT-2 as model. The calculated Bragg peaks are shown as vertical lines. The difference between the experimental data and the Rietveld refinement is shown as a blue curve below the actual data.

activation of about 10% occurs between −50 °C and 100 °C within 24 minutes. The details of the corresponding phase quantification are provided in Fig. S11 in the ESI.† This analysis confirms that in vacuum during the first stages of the initial cooling and during the first heating a gradual activation of GUT-2 occurs, which is then completed during the 12 h annealing at 100 °C.

Information about the crystallographic structure in terms of coherent crystallite size and the presence of microstrains are accessible *via* the widths of the diffraction peaks. To quantify the influence of instrumental peak broadening on our diffraction measurements, the PXRD pattern of the standard material LaB_6 was recorded under settings identical to those described in the Method Section 3.3, with measurements performed at room temperature. Extrapolation of the LaB_6 full widths at half maximum (FWHM) in the 11.6 degrees to 12.1 degrees range yielded an average of around 0.03 degrees (see Fig. S3 of the ESI† for more details), which is minimal. Therefore, no correction for instrumental broadening is needed when calculating the crystallite size. What is critical, however, is that the FWHM values are Rachinger corrected which is an iterative numerical technique that allows one to deconvolute the overlapping contributions of the $K\alpha_1$ and $K\alpha_2$ lines.[60]

During the activation/dehydration processes no change of the widths of the X-ray diffraction peaks is observed. To illustrate that, the corresponding FWHM values of several representative peaks before and after activation can be found in Tables S7–S10 (ESI†). Table 2 summarizes the obtained crystallite sizes of GUT-2 using the Scherrer equation[61] for both cooling and heating cycles. For the hydrated form the crystallite sizes (determined from the (200) reflection in the C1 and H1 series) are comparably large (111 ± 4 nm and 111 ± 3 nm, respectively). This demonstrates the good structural integrity of GUT-2 when H_2O molecules are present in the pores. In contrast, the activated form (analyzed based on the (110) reflection) shows significantly smaller crystallite sizes of 63 ± 1 nm and 69 ± 5 nm in the C1 and H1 series. Interestingly, in the second measurement set (C2 and H2), the activated form exhibits larger domains (76 ± 2 nm and 77 ± 1 nm), indicative of a structural annealing during the extended heat treatment.

3.3. Quantifying the thermal expansion and its dependence on the hydration state

The Rietveld refinements discussed in the previous section are valuable not only for phase quantifications but also for

Table 2 Estimated sizes of hydrated and activated GUT-2 crystals using the Scherrer equation[61] for both cooling (C1 and C2) and heating cycles (H1 and H2)

Measurement series	Laue indices	Crystal domain	Crystallite size [nm]
C1	(200)	Hydrated	111 ± 4
	(110)	Activated	63 ± 1
H1	(200)	Hydrated	111 ± 3
	(110)	Activated	69 ± 5
C2	(110)	Activated	76 ± 2
H2	(110)	Activated	77 ± 1

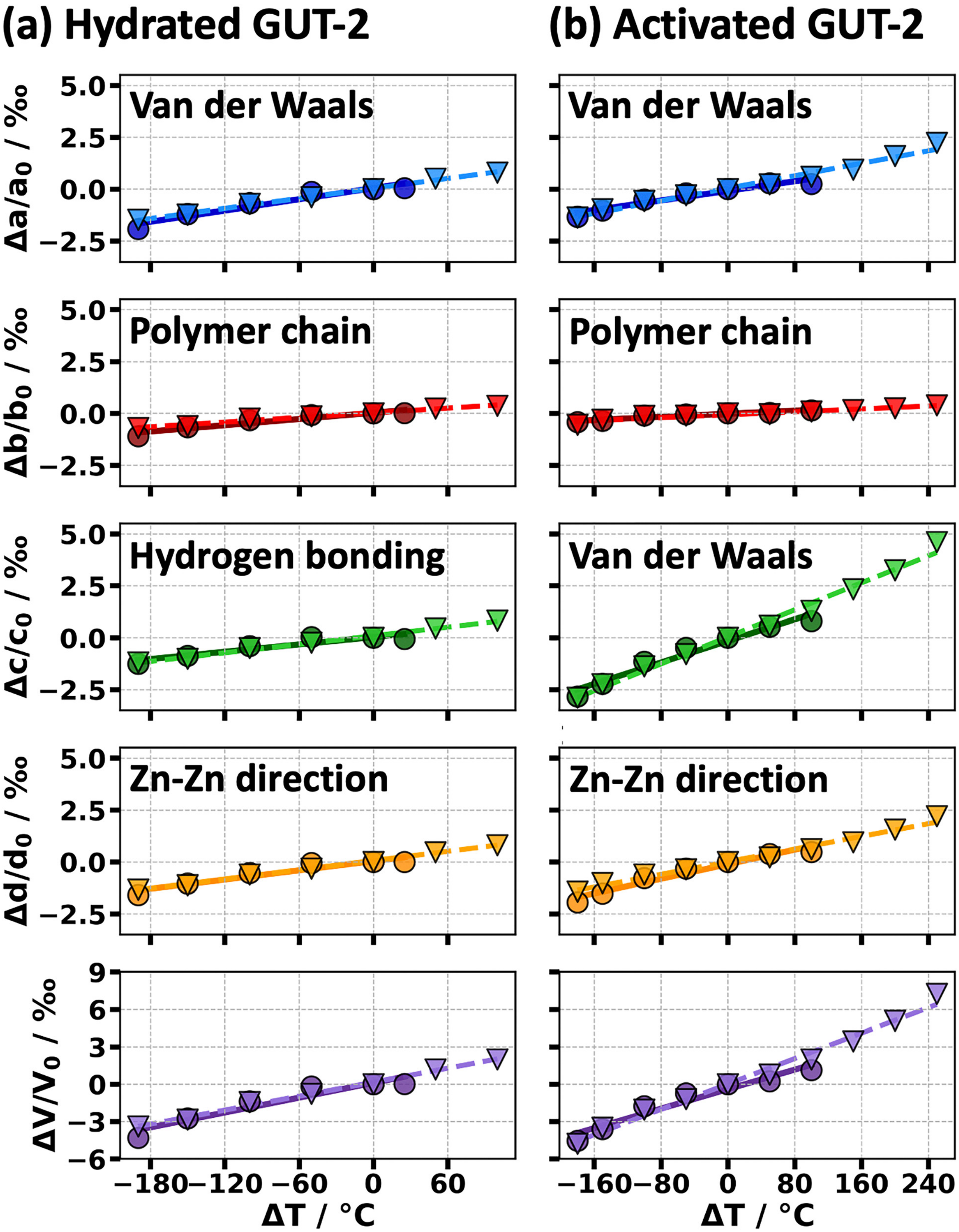

Fig. 5 Temperature-induced changes of the three cell parameters (*a*, *b* and *c*) as well as of the diagonal (*d*) and the cell volume (*V*) relative to the values measured at a temperature (*T*) of 0 °C. The data represent the situation of hydrated GUT-2 (a) and activated GUT-2 (b). The temperature change is given relative to 0 °C and the unit-cell parameters have been extracted based on Rietveld refinements. Data points represented by circles (○) correspond to cooling runs, while those shown as inverted triangles (▽) belong to heating runs. Solid lines indicate the linear fits for the cooling processes and dashed lines represent the fits for the heating processes.

Table 3 Anisotropic lattice and volumetric thermal expansion coefficients for the cooling (C1, C2) and heating curves (H1, H2) obtained *via* linear fits through the cell parameters that were determined *via* Rietveld refinements. While the data for C1 and H1 are characteristic of the hydrated form of GUT-2, C2 and H2 correspond to the fully activated GUT-2. *a*, *b*, and *c* refer to the lattice constants, *d* to the diagonal (see Fig. 1(b) and (e)) and *V* to the volume of the unit cell

		α_a [10^{-6} K^{-1}]	α_b [10^{-6} K^{-1}]	α_c [10^{-6} K^{-1}]		
		van der Waals	Polymer chain	Hydrogen bonding	α_d [10^{-6} K^{-1}]	α_V [10^{-6} K^{-1}]
Hydrated form	C1	8.94	1.24	5.87	7.41	20.0
	H1	8.01	3.74	6.88	7.45	18.8

		α_a [10^{-6} K^{-1}] van der Waals	α_b [10^{-6} K^{-1}] Polymer chain	α_c [10^{-6} K^{-1}] van der Waals	α_d [10^{-6} K^{-1}]	α_V [10^{-6} K^{-1}]
Activated form	C2	5.79	1.90	13.0	8.77	19.6
	H2	7.53	1.76	16.3	11.8	25.5

determining the anisotropic thermal expansion coefficients. Using the temperature-dependent cell parameters obtained from these refinements (shown in Fig. 4), the thermal and volumetric expansion coefficients can be calculated through the following equations:

$$\alpha_L = \left(\frac{\partial L}{\partial T}\right)_p \frac{1}{L_0} \quad \text{with } L = \{a,\ b,\ c,\ d\}$$

$$\alpha_V = \left(\frac{\partial V}{\partial T}\right)_p \frac{1}{V_0}$$

In the first equation, α_L is the linear thermal expansion coefficient, defined as the relative rate of change with temperature T of one of the three unit cell lengths in the crystallographic directions a, b and c. For reasons that will become apparent below, also the relative changes in directions parallel to the diagonals of the unit cells, d, were evaluated. As the unit cells in the two forms of GUT-2 are rotated relative to each other in the *ab*-plane (see Fig. 1(b) and (e)), the diagonals in one form essentially correspond to the unit cell directions in the other. The second of the above equations introduces the volumetric thermal expansion coefficient, α_V, which quantifies the fractional volume change with temperature. The linear thermal expansion coefficients for GUT-2 as well as the volumetric expansion coefficient are obtained from linear fits of the temperature-dependent cell parameters, as shown in a side-by-side comparison of the hydrated and activated forms in Fig. 5. L_0 and V_0 are set to the values of the temperature at 0 °C. Conceptually, also non-linear terms are expected to contribute as there is no reason to assume that the thermal expansion of GUT-2 remains exactly the same for all studied temperatures. However, the linear fits represent the experimental data rather well and the uncertainty of the individual datapoints makes fitting higher-order polynomials futile. Thus, we restrict the analysis to the linear expansion coefficients summarized in Table 2 for all cooling and heating processes.

Hydrated and activated GUT-2 show generally low volumetric thermal expansion values of around 19×10^{-6} K^{-1} to 26×10^{-6} K^{-1}. Notably, the temperature-induced volume change shows a weak hysteresis effect, especially during the cooling cycles. In its hydrated form, GUT-2 exhibits nearly ZTE along the *b*-axis, with expansion coefficients ranging from approximately 1.2×10^{-6} K^{-1} to 3.7×10^{-6} K^{-1} (compare Table 3). This direction is characterized by strong covalent bonding within the polymer chains, which significantly restricts thermal expansion due to the high bond strength and the narrow, apparently almost symmetric potential energy well associated with changing the length of *b*. A more quantitative discussion of how strong bonds typically lead to a reduced thermal expansion is provided in Section S8 in the ESI.† Concerning thermal expansion in the direction of the *c*-axis of the hydrated form, where hydrogen bonds connect the individual polymer strands, the expansion coefficient increases to around 5.9×10^{-6} K^{-1} to 6.9×10^{-6} K^{-1} reflecting the fact that hydrogen bonds are significantly weaker (and apparently more anharmonic) than covalent bonds. Finally, the *a*-axis, in which inter-chain interactions are predominantly governed by van der Waals interactions, exhibits the highest thermal expansion coefficient, reaching values of 8.0×10^{-6} K^{-1} to 8.9×10^{-6} K^{-1}. This trend is again in line with expectations, as van der Waals forces are significantly weaker than hydrogen or covalent bonds and are particularly anharmonic (considering, *e.g.*, Lenard-Jones potentials; see also discussion in Section S8, ESI†). This allows the framework to deform more easily upon heating.

Upon activation of the framework, the *b*-direction – which for our naming convention again corresponds to the polymer chain direction – continues to exhibit essentially ZTE, with values remaining close to 1.8×10^{-6} K^{-1}. Regarding thermal expansion in directions perpendicular to the chain, it is not useful to directly compare α_a and α_c between both systems due to the rotated unit cell. Instead, it is sensible to analyze the relative change of the Zn–Zn distance mentioned above, which (as illustrated in Fig. 1(e)) corresponds to the relative change of the length of the diagonals of the unit cells in the *ac*-plane, α_d. Notably, due to the orthorhombic space group the expansion coefficients for both diagonals are identical in the activated form. Interestingly, α_d of activated GUT-2 is clearly larger than α_c of the hydrated form and is in the same range as the value for the van der Waals bonding direction in the hydrated form, α_a. This is consistent with the absence of hydrogen bonds in activated GUT-2.

3.4. Crystallization kinetics

A second set of experiments was performed to assess the possibility of controlling the dehydration and rehydration process of GUT-2 under standard laboratory conditions. To probe these aspects, separate temperature-dependent PXRD measurements were carried out in air (relative humidity of 30%) rather than in vacuum (for details on the experimental setup see Method Section 3.4). Starting with the hydrated as-synthesized GUT-2 powder sample – which is identical to the sample used in previous experiments – the material was activated at a constant temperature of 50 °C and PXRD patterns were recorded every 40 minutes (reported in the first column of Fig. S12 in the ESI†). Rietveld refinements were employed to quantify this phase transformation, allowing for a quantitative tracking of the hydration state of GUT-2 as a function of time. The resulting phase fractions are displayed in Fig. 6(a). They reveal that full activation of the MOF under these conditions requires approximately 6 hours. A second experiment (Fig. S12(a), ESI†) showed that when the sample is heated to 90 °C (again in air), full activation occurs within 30 minutes.

After activation, the dehydrated GUT-2 sample was left in air at 30% humidity and at room temperature (25 °C) to explore the rehydration process. Again, PXRD measurements captured the structural changes as H_2O gradually diffused back into the framework. The corresponding phase quantifications, summarized in Fig. 6(b), show that H_2O adsorption under these conditions required nearly 2 days to reach completion.

To gain deeper insights into the mechanisms regarding H_2O uptake and release in GUT-2, we employed the Avrami equation.[62–64] It is based on a widely used phenomenological model[65–67] that describes the kinetics of isothermal phase transitions, particularly providing insights into geometrical evolutions of the crystals during the transformation process. Moreover, the model was applied to study the structural evolution of the MOFs ZIF-8[68] and ZIF-67.[69]

The Avrami equation can be written as

$$X(t) = 1 - \exp(-kt^n)$$

with $X(t)$ being the transformed volume fraction as a function of the time t, n corresponding to the Avrami exponent and k representing the reaction rate constant. The Avrami exponent

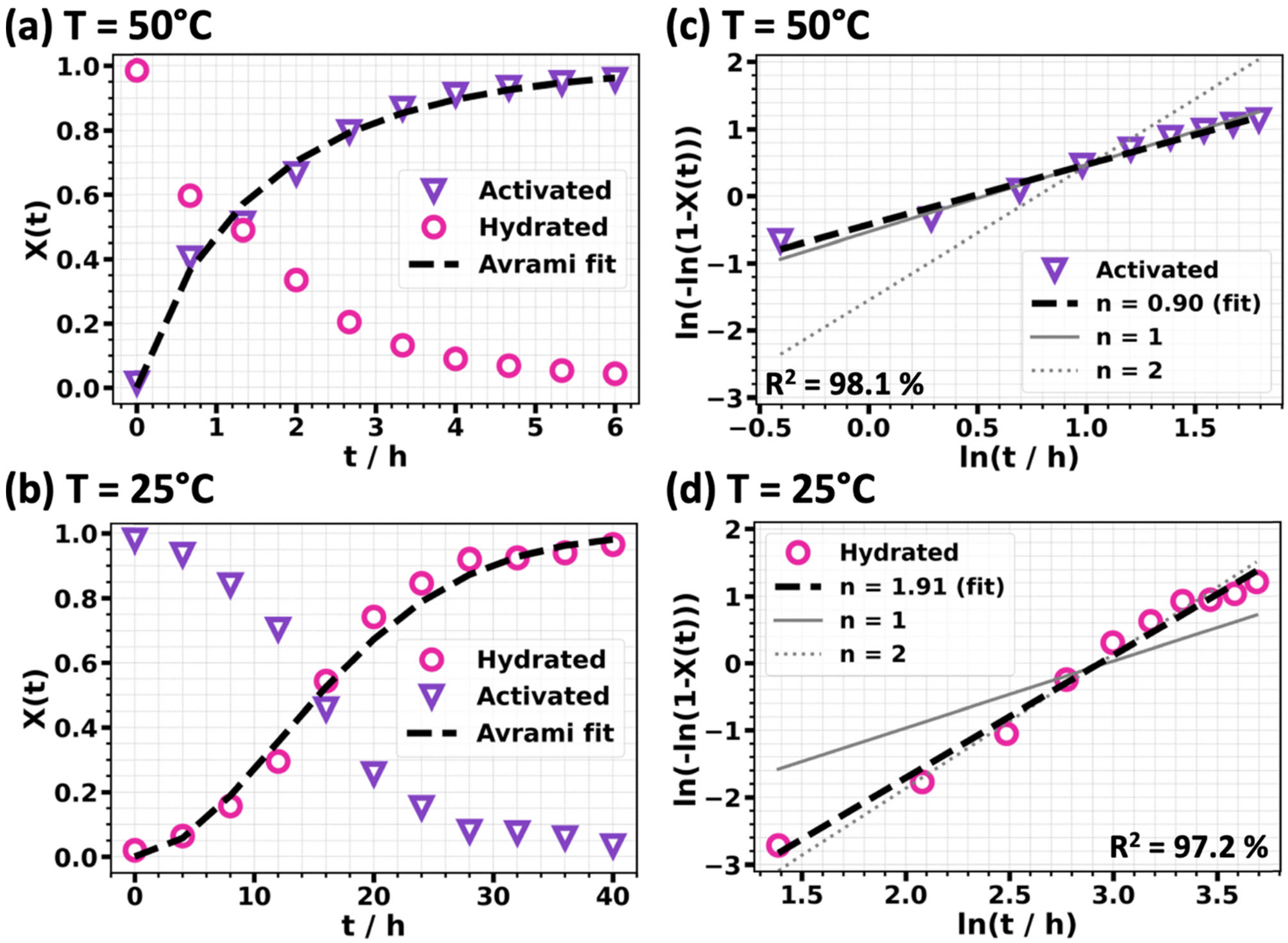

Fig. 6 Evolution of the hydration state of GUT-2 powder during the activation process at 50 °C (a) and the corresponding re-hydration process at 25 °C (b). The left panels include the resulting Avrami fit (dashed black lines) based on the extracted constants from the linearized form of the Avrami plots shown on the right-hand side. $X(t)$ denotes the fraction of the compound that has been converted at a certain time t, ranging from 0 (untransformed) to 1 (fully transformed). Data points with purple, inverted triangles (▽) belong to the activated GUT-2 phase that forms at a constant temperature of 50 °C, while data points illustrated with pink circles (○) belong to the hydrated GUT-2 phase that forms at a temperature of 25 °C. For the linear fits the coefficient of determination (R^2) is given. The solid and dashed grey lines in panels (c) and (d) represent slopes of 1 and 2, respectively, and are shown for the sake of comparison.

n has been related to the dimensionality of crystal growth[70] in particular if it assumes integer numbers.[67] While the classical formulation of the Avrami equation does not account for diffusion-controlled processes (as they occur for GUT-2 hydration and activation) the Avrami formalism still serves as an effective tool to approximate and interpret the overall transformation kinetics. In such a case, associating integer values of n with the dimensionality of the process might not always be fully justified. Nevertheless, changes in n can be interpreted as a clear indication for changes in the underlying mechanism for the growth/shrinkage of specific structures (here, during the adsorption/desorption of H_2O molecules).

To determine the Avrami exponent for the activation and rehydration of GUT-2, a linearized form of the Avrami equation is used. By plotting $\ln[-\ln(1 - X(t))]$ *versus* $\ln(t)$, the exponent n can be extracted directly from the slope of the resulting straight line. For the activation of GUT-2 at 50 °C, the Avrami exponent is determined to be 0.90, *i.e.*, slightly below 1, which would typically be interpreted as a low-dimensional process. For the rehydration of GUT-2 the exponent extracted from the fit amounts to 1.91, indicative of a mechanism with larger dimensionality than the activation process. We note that the difference in the Avrami exponents is observed for processes at different temperatures, which can have an impact on the dimensionality of the growth of adsorption/resorption sites. Moreover, the diffusion along the polymer axis (in *b*-direction; Fig. 1(b)) is hindered by adsorbed H_2O molecules, as they block the channels. In part this is also true for water diffusion along the *a*-axis (see Fig. 1(a)). This can influence activation and hydration differently, as the activation process will typically start from the surface of the crystallites and then proceeds towards their interior; upon hydration, the H_2O molecules will again first adsorb and block the channels close to the surface, but now this is expected to delay the further conversion in the interior of the crystallites as at least along two directions water-diffusion is hindered. These considerations show that it is realistic that the kinetics of hydration and activation of GUT-2 are qualitatively different (as indicated by different Avrami exponents). To what extent the dimensionality of the processes plays a role, remains, however, elusive.

4. Conclusions

In conclusion, we show that the coordination polymer GUT-2, consisting of Zn^{2+} centres connected by 3-(2-methyl-1*H*-imidazol-1-yl)propanoate linkers, can be reversibly hydrated and activated. In the hydrated form, H_2O molecules generate bridging hydrogen bonds between neighbouring polymer strands and at the same time block the pores of GUT-2 in the direction parallel to the polymer chains. Activation of GUT-2, besides breaking the hydrogen bonds between polymer chains, also triggers a modification of the pore structure such that the crystallographic unit cell is rotated in the plane perpendicular to the polymer chains. Additionally, its cell volume is reduced by more than a factor of 2 due to the concomitantly reduced number of atoms in the unit cell. The structural properties of GUT-2 are initially determined by single-crystal diffraction and subsequently confirmed by Rietveld refinement of powder data.

In the current study, GUT-2 is activated by heating crystallites either in air or in vacuum. In air and at 50 °C, full activation takes approximately six hours, while rehydration under ambient conditions and 30% relative humidity takes roughly two days. Notably, the timescales depend on the chosen conversion conditions (like the relative humidity of the atmosphere, the base pressure, or the sample temperature). An essentially instantaneous rehydration of the crystallites can be achieved by exposing them to a drop of liquid H_2O, where X-ray diffraction experiments suggest that the said rehydration processes induce a certain number of defects, but do not destroy the structural integrity of the studied materials.

Temperature-dependent X-ray diffraction experiments on suitably preconditioned samples in combination with Rietveld refinements allow the determination of the anisotropic thermal expansion coefficients of both forms of GUT-2. The results reveal an interesting correlation between the nature of the bonding interactions in a specific direction and the thermal expansion coefficient in that direction: along the polymer chains, where covalent bonds dominate, particularly small thermal expansion coefficients typically around $2 \times 10^{-6}\ \mathrm{K}^{-1}$ are observed. Thermal expansion increases by a factor of around 3 to 4 in the less strongly bonded direction dominated by hydrogen bonds (in hydrated GUT-2) and increases even somewhat further in the van der Waals bonded directions (in both forms of GUT-2). This suggests a correlation between the depths of the bonding potentials in the different directions and their degree of anharmonicity.

Finally, the Avrami equation is used to analyse the dynamics of activation and rehydration processes of GUT-2 and to gain further insights into the crystal formation. Interestingly, we find distinctly different Avrami exponents for the kinetics of the activation and hydration processes, which suggests fundamental differences between them. This is associated to the blocking of pores in polymer direction by adsorbed H_2O molecules. Especially for the rehydration, this partially blocks the access of water molecules to the interior of the crystallites.

Our findings demonstrate that minor changes in the hydration state of a coordination polymer or MOF can lead to significant functional adaptations in the properties of the studied materials. The results provide a compelling case for the strategic use of guest molecules to modulate the properties of porous frameworks.

Author contributions

Conceptualization: E. Z., R. R., C. S., N. S.; formal analysis: N. S.; funding acquisition: E. Z., R. R.; investigation: N. S., B. S., S. J., B. K., A. T., F. P. L.; resources: E. Z., R. R., C. S.; software: B. B., A. T., N. S., F. P. L.; supervision: E. Z., R. R.; visualization: N. S., F. P. L.; writing – original draft: N. S.; writing – review & editing: E. Z., R. R.

Conflicts of interest

There are no conflicts to declare.

Data availability

The data generated in this work will be made available at the TU Graz Repository upon acceptance by a peer-reviewed journal: **https://doi.org/10.3217/tst5n-0d276**.

Acknowledgements

This research was funded in part by the Graz University of Technology through the Lead Project Porous Material @ Work for Sustainability (LP-03). This research was primarily funded by the Austrian Science Fund (FWF) [10.55776/P34463]. For the purpose of open access, the author has applied a CC-BY public copyright license to any Author Accepted Manuscript version arising from this submission. The computational results have been achieved using the Austrian Scientific Computing (ASC) infrastructure.

References

1 S. R. Batten, N. R. Champness, X.-M. Chen, J. Garcia-Martinez, S. Kitagawa, L. Öhrström, M. O'Keeffe, M. Paik Suh and J. Reedijk, *Pure Appl. Chem.*, 2013, **85**, 1715–1724.
2 V. Pascanu, G. González Miera, A. K. Inge and B. Martín-Matute, *J. Am. Chem. Soc.*, 2019, **141**, 7223–7234.
3 D. Yang and B. C. Gates, *ACS Catal.*, 2019, **9**, 1779–1798.
4 L. Jiao and H.-L. Jiang, *Chin. J. Catal.*, 2023, **45**, 1–5.
5 W. Liang, P. Wied, F. Carraro, C. J. Sumby, B. Nidetzky, C.-K. Tsung, P. Falcaro and C. J. Doonan, *Chem. Rev.*, 2021, **121**, 1077–1129.
6 H. D. Lawson, S. P. Walton and C. Chan, *ACS Appl. Mater. Interfaces*, 2021, **13**, 7004–7020.
7 T. Burger, M. V. Hernández, C. Carbonell, J. Rattenberger, H. Wiltsche, P. Falcaro, C. Slugovc and S. M. Borisov, *ACS Appl. Nano Mater.*, 2023, **6**, 248–260.
8 L. Zhang, Y. Zhou and S. Han, *Angew. Chem., Int. Ed.*, 2021, **60**, 15192–15212.
9 L. Bellarosa, J. M. Castillo, T. Vlugt, S. Calero and N. López, *Chem. – Eur. J.*, 2012, **18**, 12260–12266.
10 H. Li, M. Eddaoudi, M. O'Keeffe and O. M. Yaghi, *Nature*, 1999, **402**, 276–279.
11 Y. Ming, N. Kumar and D. J. Siegel, *ACS Omega*, 2017, **2**, 4921–4928.
12 N. Hanikel, X. Pei, S. Chheda, H. Lyu, W. Jeong, J. Sauer, L. Gagliardi and O. M. Yaghi, *Science*, 2021, **374**, 454–459.
13 W. Song, Z. Zheng, A. H. Alawadhi and O. M. Yaghi, *Nat. Water*, 2023, **1**, 626–634.
14 J. Canivet, A. Fateeva, Y. Guo, B. Coasne and D. Farrusseng, *Chem. Soc. Rev.*, 2014, **43**, 5594–5617.
15 H. Furukawa, F. Gándara, Y.-B. Zhang, J. Jiang, W. L. Queen, M. R. Hudson and O. M. Yaghi, *J. Am. Chem. Soc.*, 2014, **136**, 4369–4381.
16 M. R. Momeni, Z. Zhang, D. Dell'Angelo and F. A. Shakib, *Phys. Chem. Chem. Phys.*, 2021, **23**, 3135–3143.
17 H. Tanaka, S. Ohsaki, S. Hiraide, D. Yamamoto, S. Watanabe and M. T. Miyahara, *J. Phys. Chem. C*, 2014, **118**, 8445–8454.
18 T. Kamencek, B. Schrode, R. Resel, R. Ricco and E. Zojer, *Adv. Theory Simul.*, 2022, **5**, 2200031.
19 S. R. Madsen, N. Lock, J. Overgaard and B. B. Iversen, *Acta Crystallogr., Sect. B: Struct. Sci., Cryst. Eng. Mater.*, 2014, **70**, 595–601.
20 S. R. G. Balestra, R. Bueno-Perez, S. Hamad, D. Dubbeldam, A. R. Ruiz-Salvador and S. Calero, *Chem. Mater.*, 2016, **28**, 8296–8304.
21 A. Shrivastava, T. Sethi and D. Das, *Cryst. Growth Des.*, 2022, **22**, 3479–3484.
22 Y. Wu, A. Kobayashi, G. J. Halder, V. K. Peterson, K. W. Chapman, N. Lock, P. D. Southon and C. J. Kepert, *Angew. Chem., Int. Ed.*, 2008, **47**, 8929–8932.
23 L. H. N. Rimmer, M. T. Dove, A. L. Goodwin and D. C. Palmer, *Phys. Chem. Chem. Phys.*, 2014, **16**, 21144–21152.
24 Q. Gao, Y. Jiao and G. Li, *Chin. Phys. B*, 2022, **31**, 046501.
25 T. Kamencek and E. Zojer, *J. Phys. Chem. C*, 2021, **125**, 24728–24745.
26 K. Lin, W. Zhang, C. Yu, Q. Sun, Y. Cao, W. Li, S. Jiang, Q. Li, Q. Zhang, K. An, Y. Chen, D. Yu, J. Liu, K. Kato, Q. Zhang, L. Gu, X. Kuang, Y. Tang, J. Miao and X. Xing, *Cell Rep. Phys. Sci.*, 2023, **4**, 101254.
27 Z. Tan, P. Miao, M. Hagihala, S. Lee, Y. Ishikawa, S. Torii, M. Yonemura, T. Saito, S. Deng, J. Chen, L. He, R. Du, J. Zhang, H. Li, J. Sun, Y. Wang, X. Lin, K. Li and T. Kamiyama, *J. Phys. Chem. Lett.*, 2020, **11**, 6785–6790.
28 H. L. B. Boström, S. Bette, S. T. Emmerling, M. W. Terban and B. V. Lotsch, *APL Mater.*, 2022, **10**, 071106.
29 A. Gładysiak, S. M. Moosavi, L. Sarkisov, B. Smit and K. C. Stylianou, *CrystEngComm*, 2019, **21**, 5292–5298.
30 Y. Kim, R. Haldar, H. Kim, J. Koo and K. Kim, *Dalton Trans.*, 2016, **45**, 4187–4192.
31 A. Gładysiak, S. M. Moosavi, L. Sarkisov, B. Smit and K. C. Stylianou, *CrystEngComm*, 2019, **21**, 5292–5298.
32 Y. Kim, R. Haldar, H. Kim, J. Koo and K. Kim, *Dalton Trans.*, 2016, **45**, 4187–4192.
33 E. J. Carrington, R. Pétuya, R. K. Hylton, Y. Yan, D. Antypov, G. R. Darling, M. S. Dyer, N. G. Berry, A. P. Katsoulidis and M. J. Rosseinsky, *Cryst. Growth Des.*, 2019, **19**, 5604–5618.
34 H. L. B. Boström, S. Bette, S. T. Emmerling, M. W. Terban and B. V. Lotsch, *APL Mater.*, 2022, **10**, 071106.
35 K. Kodolitsch, A. Torvisco, T. Kamencek, M. Mazaj, E. Zojer and C. Slugovc, *Eur. J. Inorg. Chem.*, 2025, e202500032.
36 *CrysAlisPro Software System (version 1.171.43.92a) Rigaku Oxford Diffraction*, 2023.
37 O. V. Dolomanov, L. J. Bourhis, R. J. Gildea, J. A. K. Howard and H. Puschmann, *J. Appl. Crystallogr.*, 2009, **42**, 339–341.
38 G. M. Sheldrick, *Acta Crystallogr., Sect. A: Found. Adv.*, 2015, **71**, 3–8.
39 G. M. Sheldrick, *Acta Crystallogr., Sect. A: Found. Crystallogr.*, 2008, **64**, 112–122.

40 F. H. Allen, O. Johnson, G. P. Shields, B. R. Smith and M. Towler, *J. Appl. Crystallogr.*, 2004, **37**, 335–338.

41 S. P. Westrip, *J. Appl. Crystallogr.*, 2010, **43**, 920–925.

42 H. M. Rietveld, *J. Appl. Crystallogr.*, 1969, **2**, 65–71.

43 T. Degen, M. Sadki, E. Bron, U. König and G. Nénert, *Powder Diffr.*, 2014, **29**, S13–S18.

44 G. Caglioti, A. Paoletti and F. P. Ricci, *Nucl. Instrum.*, 1958, **3**, 223–228.

45 G. Caglioti, A. Paoletti and F. P. Ricci, *Nucl. Instrum. Methods*, 1960, **9**, 195–198.

46 C. Caglioti and F. P. Ricci, *Nucl. Instrum. Methods*, 1962, **15**, 155–163.

47 W. A. Dollase, *J. Appl. Crystallogr.*, 1986, **19**, 267–272.

48 P. Niggli, *Kristallographische und strukturtheoretische Grundbegriffe. Handbuch der Experimentalphysik*, Akademische Verlagsgesellschaft, Leipzig, Part 1, 1928, vol. 7.

49 R. Resel, E. Tamas, B. Sonderegger, P. Hofbauer and J. Keckes, *J. Appl. Crystallogr.*, 2003, **36**, 80–85.

50 C. F. Macrae, P. R. Edgington, P. McCabe, E. Pidcock, G. P. Shields, R. Taylor, M. Towler and J. van de Streek, *J. Appl. Crystallogr.*, 2006, **39**, 453–457.

51 F. Formalik, A. V. Neimark, J. Rogacka, L. Firlej and B. Kuchta, *J. Colloid Interface Sci.*, 2020, **578**, 77–88.

52 A. Boutin, F.-X. Coudert, M.-A. Springuel-Huet, A. V. Neimark, G. Férey and A. H. Fuchs, *J. Phys. Chem. C*, 2010, **114**, 22237–22244.

53 L. J. Barbour, *Chem. Commun.*, 2006, 1163.

54 B. Lee and F. M. Richards, *J. Mol. Biol.*, 1971, **55**, 379-IN4.

55 F. Mouhat and F.-X. Coudert, *Phys. Rev. B: Condens. Matter Mater. Phys.*, 2014, **90**, 224104.

56 F. P. Lindner, N. Strasser, M. Schultze, S. Wieser, C. Slugovc, K. Elsayad, K. J. Koski, E. Zojer and C. Czibula, *J. Phys. Chem. Lett.*, 2025, **16**, 1213–1220.

57 A. Van Der Lee and D. G. Dumitrescu, *Chem. Sci.*, 2021, **12**, 8537–8547.

58 Y. Iwai, S. Kusumoto, R. Suzuki, M. Tachibana, K. Komatsu, T. Kikuchi, S. I. Kawaguchi, H. Kadobayashi, Y. Masubuchi, Y. Yamamoto, Y. Ozawa, M. Abe, K. Hirai, B. Le Ouay, M. Ohba and R. Ohtani, *Chem. Mater.*, 2024, **36**, 5446–5455.

59 P. Müller, R. Herbst-Irmer, A. L. Spek, T. R. Schneider and M. R. Sawaya, *Crystal Structure Refinement: A Crystallographer's Guide to SHELXL*, Oxford University Press, New York, United States, 2006.

60 W. A. Rachinger, *J. Sci. Instrum.*, 1948, **25**, 254.

61 P. Scherrer, *Kolloidchemie Ein Lehrbuch*, Springer Berlin Heidelberg, Berlin, Heidelberg, 1912, pp. 387–409.

62 M. Avrami, *J. Chem. Phys.*, 1939, **7**, 1103–1112.

63 M. Avrami, *J. Chem. Phys.*, 1940, **8**, 212–224.

64 M. Avrami, *J. Chem. Phys.*, 1941, **9**, 177–184.

65 K. Shirzad and C. Viney, *J. R. Soc., Interface*, 2023, **20**, 20230242.

66 M. Fanfoni and M. Tomellini, *Il Nuovo Cimento D*, 1998, **20**, 1171–1182.

67 M. M. Moghadam and P. W. Voorhees, *Scr. Mater.*, 2016, **124**, 164–168.

68 S. R. Venna, J. B. Jasinski and M. A. Carreon, *J. Am. Chem. Soc.*, 2010, **132**, 18030–18033.

69 X. Feng and M. A. Carreon, *J. Cryst. Growth*, 2015, **418**, 158–162.

70 Q. Liu, J. Shi, S. Zheng, M. Tao, Y. He and Y. Shi, *Ind. Eng. Chem. Res.*, 2014, **53**, 11677–11683.